



Mg doping induced high structural quality of sol-gel ZnO nanocrystals: Application in photocatalysis

Chayma Abed^a, Chaker Bouzidi^a, Habib Elhouichet^{a,b,*}, Bernard Gelloz^c, Mokhtar Ferid^a

^a Laboratoire de Physico-chimie des Matériaux Minéraux et leurs Applications, Centre National de Recherches en Sciences des Matériaux, BP 95, Hammam-Lif 2050, Tunisia

^b Département de Physique, Faculté des Sciences de Tunis, Université Tunis El Manar, Tunis 2092, Tunisia

^c Graduate School of Engineering, Nagoya University, 2-24-16 Furo-cho, Chikusa-ku, Nagoya, Aichi 464-8603, Japan



ARTICLE INFO

Article history:

Received 9 February 2015

Received in revised form 12 May 2015

Accepted 14 May 2015

Available online 21 May 2015

Keywords:

ZnO NPs

Sol-gel method

Optical properties

Photocatalysis

ABSTRACT

Undoped and Mg doped ZnO nanocrystals (NCs) $\text{ZnO}:x\%\text{Mg}$ ($x = 1, 2, 3$, and 5) were synthesized using sol-gel method. The structural and optical properties were investigated by X-ray diffraction (XRD), Raman spectroscopy, diffuse reflectivity, and photoluminescence (PL). XRD analysis demonstrates that all prepared samples present pure hexagonal wurtzite structure without any Mg related phases. The NCs size varies from 26.82 nm to 42.96 nm with Mg concentrations; it presents an optimal value for 2% of Mg. The Raman spectra are dominated by the $E_{2\text{high}}$ mode. For highly Mg doping (5%), the occurrence of silent $B_{1(\text{low})}$ mode suggested that the Mg ions do substitute at Zn sites in the ZnO lattice. The band gap energy was estimated from both Tauc and Urbach methods and found to be 3.39 eV for $\text{ZnO}:2\%\text{Mg}$. The PL spectra exhibit two emission bands in the UV and visible range. Their evolution with Mg doping reveals the reduction of defect density in ZnO at low Mg doping by filling Zn vacancies.

In addition, it was found that further Mg doping, above 2%, improves the photocatalytic activity of ZnO NCs for photodegradation of Rhodamine B (RhB) under sunlight irradiation. The efficient electron-hole separation is the main factor responsible for the enhancement of photocatalytic performance of Mg doped ZnO NCs.

Through this work, we show that by varying the Mg contents in ZnO, this material can be a potential candidate for both optoelectronic and photocatalytic applications.

© 2015 Elsevier B.V. All rights reserved.

1. Introduction

ZnO is n-type semiconductor material with a wide band gap of 3.3 eV and a large exciton binding energy of 60 meV [1]. ZnO has been widely studied and used for various applications such as catalysts, gas sensors, thin film-based electronic and electro-optic devices, and varistors [2,3]. ZnO can be alloyed with other high optical band gap II-VI compounds like magnesium oxide (MgO) to increase its band gap. $\text{ZnO}:\text{Mg}$ is a semiconductor composed of two materials, zinc oxide and magnesium oxide, which can be easily controlled over a wide range of temperatures because the ionic radius of Mg^{2+} and Zn^{2+} are similar [4], as a result, the incorporation

of Mg^{2+} in ZnO is not expected to induce significant change of lattice sizes [5].

Improvements in $\text{ZnO}:\text{Mg}$ dopant technology [6] led to many new applications in electronics and optoelectronics [7]. Mg has been chosen as a dopant because a large number of reports indicate the enhancement of the band gap of the ZnO by doping it with different concentrations of Mg [8].

A number of different techniques have been used to elaborate $\text{Zn}_{1-x}\text{Mg}_x\text{O}$, such as molecular beam epitaxy (MBE) [9], metalorganic vapor-phase epitaxy (MOVPE) [10], radio frequency (rf) magnetron sputtering [11], spray pyrolysis [12], pulsed laser deposition [13], chemical vapor deposition [14], electro-deposition [15], the sol-gel method technique [16]. Among these methods, the sol-gel method is an attractive process due to the simplicity, reproducibility, and controllability of compositions.

The aim of this work is to evaluate the effect of Mg doping on the microstructure and optical properties of ZnO nanocrystals grown from sol-gel method. The photocatalytic activity of $\text{ZnO}:\text{Mg}$

* Corresponding author at: Département de Physique, Faculté des Sciences de Tunis, Université Tunis El Manar, Tunis 2092, Tunisia. Tel.: +216 97632109; fax: +216 71885073.

E-mail address: Habib.elhouichet@fst.rnu.tn (H. Elhouichet).

NCs was studied by analyzing the photodegradation of RhB under sunlight irradiation.

2. Experimental details

2.1. Synthesis

The typical synthesis procedure for pure and Mg-doped ZnO is as follow: The sol was prepared using zinc acetate dehydrate [$\text{Zn}(\text{CH}_3\text{COO})_2 \cdot 2\text{H}_2\text{O}$; 0.02 M] and magnesium chloride ($\text{MgCl}_2 \cdot 2\text{H}_2\text{O}$) as the starting materials, de-ionized water as the solvent, and citric acid ($\text{C}_6\text{H}_8\text{O}_7$) as the stabilizer. The precursor solution was mixed with a magnetic stirrer in 50 °C for 2 h. The sol was pre-heated in a furnace at 80 °C for 7 days to evaporate the solvent and remove the organic residuals. A heat treatment was carried out at 350 °C for 3 h. The powders obtained from the dried sol were then annealed at 500 °C for 3 h at ambient air. Pure ZnO was also prepared by the same procedure without the addition of magnesium chloride. The doping concentrations of magnesium are expressed in at.%.

2.2. Characterization

The XRD were performed using Philips X'Pert diffractometer supplied with copper X-ray tube ($\lambda = 1.5406 \text{ \AA}$), at 40 kV and 100 mA. The intensity was determined in the range $20^\circ < 2\theta < 70^\circ$ and changes with a step size of 0.02°. Micro Raman measurements were carried out using a HORIBA Jobin Yvon spectrometer Raman LABRAM HR. The samples were excited at 325 nm by a He–Cd laser and at 632.8 nm by a He–Ne laser. Optical diffuse reflectance spectrum measurements were recorded on a PerkinElmer Lambda 900 UV-vis spectrophotometer. A sampling interval of 3 nm for this measurement was adopted to record the spectra from 250 nm to 900 nm. All measurements were made at room temperature.

2.3. Measurement of photocatalytic activity

The photocatalytic activity of Mg-doped ZnO nanopowder was investigated by measuring the photodegradation rate of RhB, as the model of organic pollutant. Experiments were performed under sunlight illumination in October in Tunis, where the temperature was about 27 °C. 10 mg of the prepared sample is added to 40 ml of RhB aqueous solution with an initial concentration of 5×10^{-6} M. The above reaction mixture was magnetically stirred for 15 min in dark to obtain a homogenous dispersion and reach the adsorption equilibrium. The solution is taken in beaker covered with thin plastic sheet to avoid evaporation of the dye solution under sunlight and it is magnetically stirred throughout the photocatalytic experiment. The absorption spectra were recorded between 400 nm and 650 nm. The absorbance (A_t) of the decomposed RhB was measured every 20 min. The photocatalytic performance was determined by the decrease of the absorption of the dye as a function of irradiation time and the concentration of Mg.

3. Results and discussion

3.1. X-ray diffraction

Fig. 1A shows the XRD patterns of $\text{ZnO}:x\%\text{Mg}$ ($x = 1, 2, 3, 5$) NCs annealed at 500 °C, in the range of $2\theta = 20^\circ$ – 70° . They indicate the single phase formation with hexagonal wurtzite structure for all ZnO NCs. The three pronounced diffraction peaks at about $2\theta = 31.8^\circ, 34.5^\circ$, and 36.3° are identified, respectively, as the (1 0 0), (0 0 2), and (1 0 1) peaks of ZnO [17,18]. All the diffraction peaks in the patterns belong to wurtzite ZnO, with high quality crystalline and a preferred orientation in (1 0 1) plane. The hexagonal structure is not changed during the doping, but it can be seen from **Fig. 1B** that the incorporation of Mg^{2+} ions affects the intensity of the preferred orientation peak, so it enhances the crystalline quality. The $\text{ZnO}:2\%\text{Mg}$ sample shows the intense and the narrower peaks which indicate its good crystallinity. It can be seen from the XRD patterns that there are no peaks related to Mg compounds which may indicate the incorporation of Mg ions into the ZnO lattice site. The ionic radius of Mg^{2+} (0.057 nm) is quite close to that of Zn^{2+} (0.060 nm) so the incorporation of Mg^{2+} ions in the ZnO lattice is possible and Mg-doped ZnO materials are found to be a single phase alloy in a wide range of Mg doping levels. In addition, the lattice parameters are not influenced by the concentration of Mg doping (**Table 1**).

There are a number of methods used to calculate the effect of lattice strain on broadening of the lattice diffraction peaks such as the Williamson–Hall and the size strain plot methods [19].

The average crystal size of the samples is calculated after appropriate background correction from X-ray line broadening of the diffraction peaks of (1 0 0), (0 0 2), and (1 0 1) planes using Debye Scherrer's formula [20].

The crystalline structures of powders are shown depending on the increasing of magnesium content. Indeed, the intensity of the preferred orientation (1 0 1) increases gradually with increasing of Mg content from 0% to 2%, as it is shown in **Fig. 1B**, the width of this peak is also affected; it evolves in the opposite way. For the optimal concentration of Mg, the preferred orientation peak is the strongest and the narrowest; the most important fact that affects the width is the lattice strain which is estimated from [21].

The crystallite size and the lattice strain values for all samples are presented in **Table 1**. It is clear that the average crystallite size is increased from 26.82 nm for undoped ZnO to 42.96 nm for ZnO doped 2%Mg. Beyond this later concentration, the crystallite size decreases with the Mg doping. The XRD spectrum of $\text{ZnO}:2\%\text{Mg}$ sample shows that the preferred orientation peak is the strongest and the narrowest compared to the (1 0 1) peaks of the other samples, it has the minimum FWHM (0.0038 radians) and the largest crystallite size (42.96 nm). **Fig. 2** shows the variation of crystallite size and the FWHM with Mg content. The increase of crystallite size is due to the fact that incorporation of magnesium atoms in the ZnO lattice causes substitution of Mg^{2+} ions with Zn^{2+} sites. This operation stops when the interstitial Zn are all replaced by Mg^{2+} , which

Table 1
The 2θ value of the preferred orientation, the corresponding FWHM value, “a” and “c” parameters (\AA), c/a , average crystallite size (D), strain (ε), d_{hkl} value, and cell volume of $\text{Zn}_{1-x}\text{Mg}_x\text{O}$ ($x = 0, 0.01, 0.02, 0.03$, and 0.05) NPs.

Sample	ZnO	0.01-MgZnO	0.02-MgZnO	0.03-MgZnO	0.05-MgZnO
2θ value (°)	36.311	36.294	36.379	36.294	36.277
FWHM (rad)	0.0060	0.0054	0.0038	0.0044	0.0048
a (\AA)	3.2498	3.2501	3.2427	3.2490	3.2501
c (\AA)	5.2066	5.2071	5.1948	5.2052	5.2071
c/a	1.6021	1.6021	1.6020	1.6021	1.6021
D (nm)	26.82	30.47	42.96	36.75	33.69
Strain ε	0.0044	0.0039	0.0028	0.0033	0.0035
Cell volume (\AA^3)	54.9879	55.0034	54.6239	54.9461	55.0033

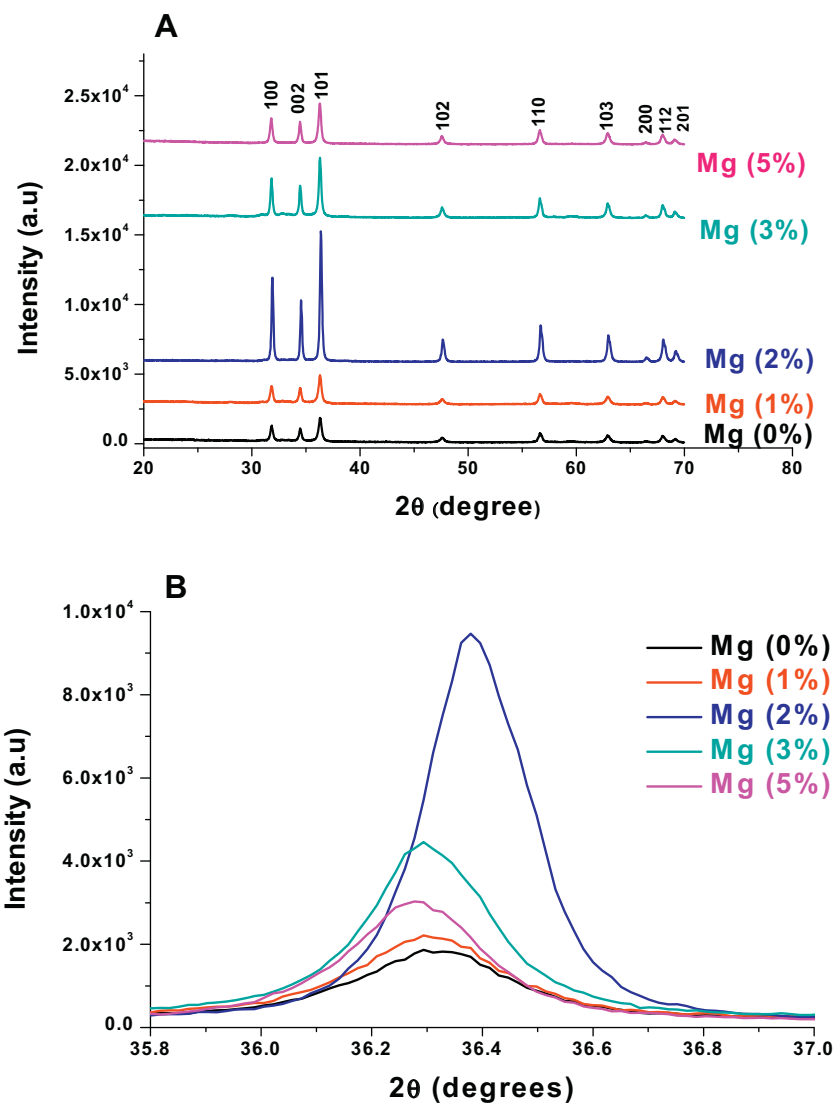


Fig. 1. (A) X-ray diffraction patterns of ZnO: $x\%$ Mg nanoparticles annealed at 500 °C. (B) Evolution of the preferred orientation peak (1 0 1) with various Mg concentrations.

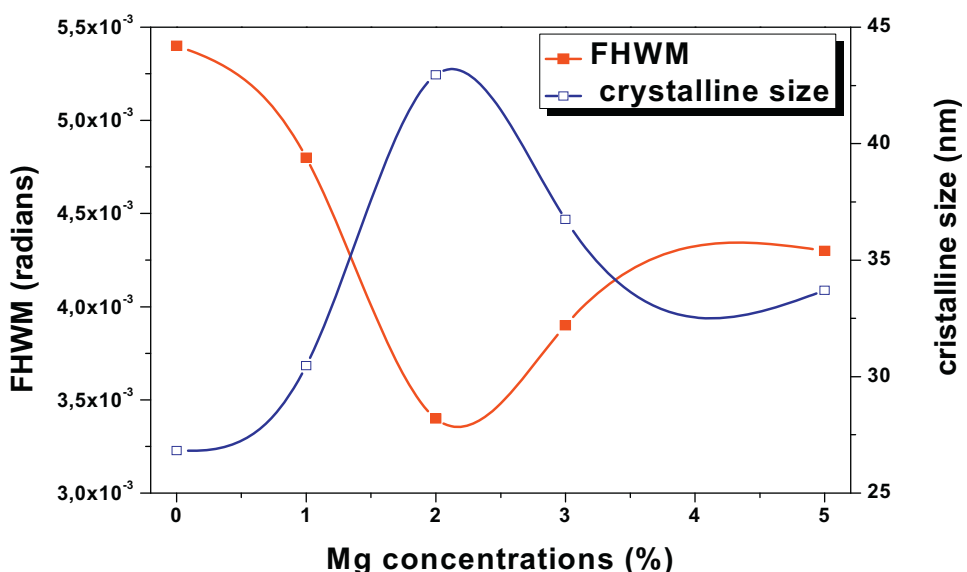


Fig. 2. The variation of FWHM and crystalline size of ZnO NPs with different Mg concentrations.

Table 2

The crystalline size D (nm) and the strain obtained by the Williamson–Hall plot method of the $Zn_{1-x}Mg_xO$ system.

Sample	ZnO	0.01-MgZnO	0.02-MgZnO	0.03-MgZnO	0.05-MgZnO
Crystallite size D (nm)	45	54	92	69	61
Strain ε	0.0019	0.0018	0.0016	0.0017	0.0018

Table 3

Full width at half maximum intensity, I_{2LO}/I_{1LO} ratio of (1LO) peak of the ZnO and Mg doped ZnO.

Sample	ZnO	0.01-MgZnO	0.02-MgZnO	0.03-MgZnO	0.05-MgZnO
FWHM (cm ⁻¹)	37.26	43.73	37.81	42.75	56.25
I_{1LO}/I_{2LO}	1.79	1.60	2.22	1.82	1.59

corresponds to the optimal concentration of doping (2% of Mg). The lattice strain values show the inverse trend of the crystallite size as it decreased up to 2% of Mg contents and then increases.

Lattice strain is a measure of the distribution of lattice constants arising from crystal imperfections, such as lattice dislocations. It was calculated from the Williamson–Hall (W–H) method. The particle size D and strain contributions ε are dependent to each other by the formula [21]:

$$\beta \cos \theta = \frac{k\lambda}{D} + 4\varepsilon \sin \theta \quad (1)$$

A plot is drawn with $(4\sin \theta)$ along the x -axis and $(\beta \cos \theta)$ along the y -axis for ZnO NPs as shown in Fig. 3. The average size is deduced from the y -axis intercept and the strain is determined from the slope of the fit. The obtained results (Table 2) show also an increase (till 2%Mg) then a decrease of the crystallite size with Mg contents. The lattice stress presents similar evolution, with Mg contents, than that obtained from Debye Scherrer's formula.

3.2. Raman spectroscopy

ZnO crystallizes in the wurtzite structure. It belongs to the space group C_{6V}^4 . The optical phonons at Γ point of the Brillouin zone belong to the following irreducible representation:

$I_{opt} = 1A_1 + 2B_1 + E_1 + 2E_2$ [22], classified as $A_1 + E_1 + 2E_2$ modes (Raman active), $2B_1$ modes (Raman silent), and $A_1 + E_1$ modes (infrared active). Moreover, the A_1 and E_1 modes split into LO and TO components. The Raman spectra of ZnO NCs were recorded for both the 325 nm and 632.8 nm excitation wavelengths from the He–Cd laser and He–Ne laser, respectively.

For the UV excitation, all the Raman spectra show three main peaks that correspond to different orders of the LO vibration mode

(Fig. 4A). The spectra are dominated by the 1LO band which is centered at about 560 cm^{-1} , the second and the third overtones are located at about 1127 cm^{-1} and 1700 cm^{-1} . The Raman spectra seem to be dependent on the quality of the synthesized NCs. The ZnO:2%Mg sample presents the highest value of the I_{1LO}/I_{2LO} ratio and the lower FWHM of 1LO Raman band (Table 3). This is an indication of the better crystalline quality of the sample ZnO:2%Mg compared to the other samples. Therefore, the defect density and the lattice stress are minimal for this sample.

For excitation with 632.8 nm wavelength, all the Raman spectra show the presence of a strong peak located at 434 cm^{-1} , assigned to the E_{2High} mode representing the band characteristic of the hexagonal wurtzite phase [23] (Fig. 4B). Raman features characteristics of Mg related phases were not observed [24]. The broad peak at about 330 cm^{-1} is attributed to the second order Raman processes involving acoustic phonons. Its presence proves a good crystalline quality of all the samples [25]. The peak at 378 cm^{-1} corresponds to A_1 (TO) [26]. Information about structural modifications could be concluded principally from the line shape, line width and asymmetry variation of the E_2 mode. The Raman mode frequency and the peak width can be influenced by the random substitution of Zn with Mg through the compositional disorder effect [27]. The corresponding band does not present any shift with Mg doping. However, it is FWHM decreases and then increases with Mg doping.

For the highly doped sample (5%Mg), a weak anomalous Raman mode appears around 271 cm^{-1} . It can be attributed to silent B_1 (low) mode in wurtzite ZnO [28]. In fact, the high Mg doping can slightly distort the ZnO lattice and break down the selection rules for the disordered system [28], which activate the intrinsic Raman modes that are normally forbidden or silent in wurtzite ZnO lattice. This suggested that the Mg ions do substitute at Zn sites in the ZnO lattice.

The absence of extra-vibrational modes corresponding to some secondary phase confirms the successful doping of Mg into the hexagonal wurtzite structure of ZnO NCs. Also, the fact that the peak positions in Raman spectra are unchanged after doping, it can indicate that Mg doping causes little distortion in the ZnO lattice. These results are consistent with those of XRD.

3.3. UV-vis measurements

Diffuse reflectance spectroscopy was used in this work to characterize the band gap and the energy structures of Mg doped ZnO NCs. The absorption coefficient α is deduced from the Kubelka–Munk function [29].

Using the Tauc relationship [30], the optical band gap E_g is determined for all ZnO samples. It is found that the band gap energy E_g of ZnO NCs increases slightly after Mg doping till 2% (Table 4) maybe the large increase of the size. This may be attributed to the incorporation of doping atoms in contrast to the size effect since it has negligible influence on the band structure of ZnO NPs for diameter

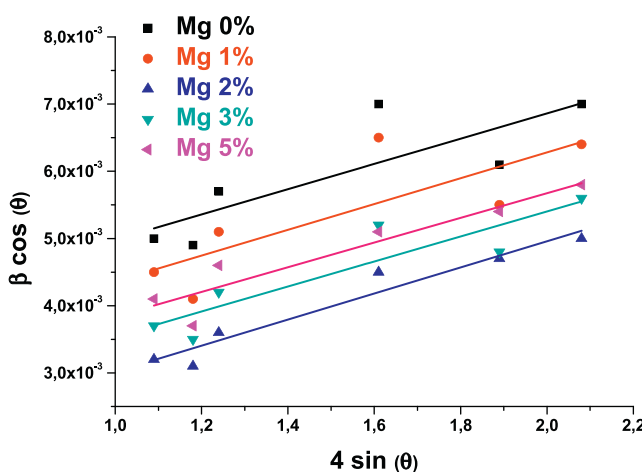


Fig. 3. Size strain method of ZnO and Mg doped ZnO.

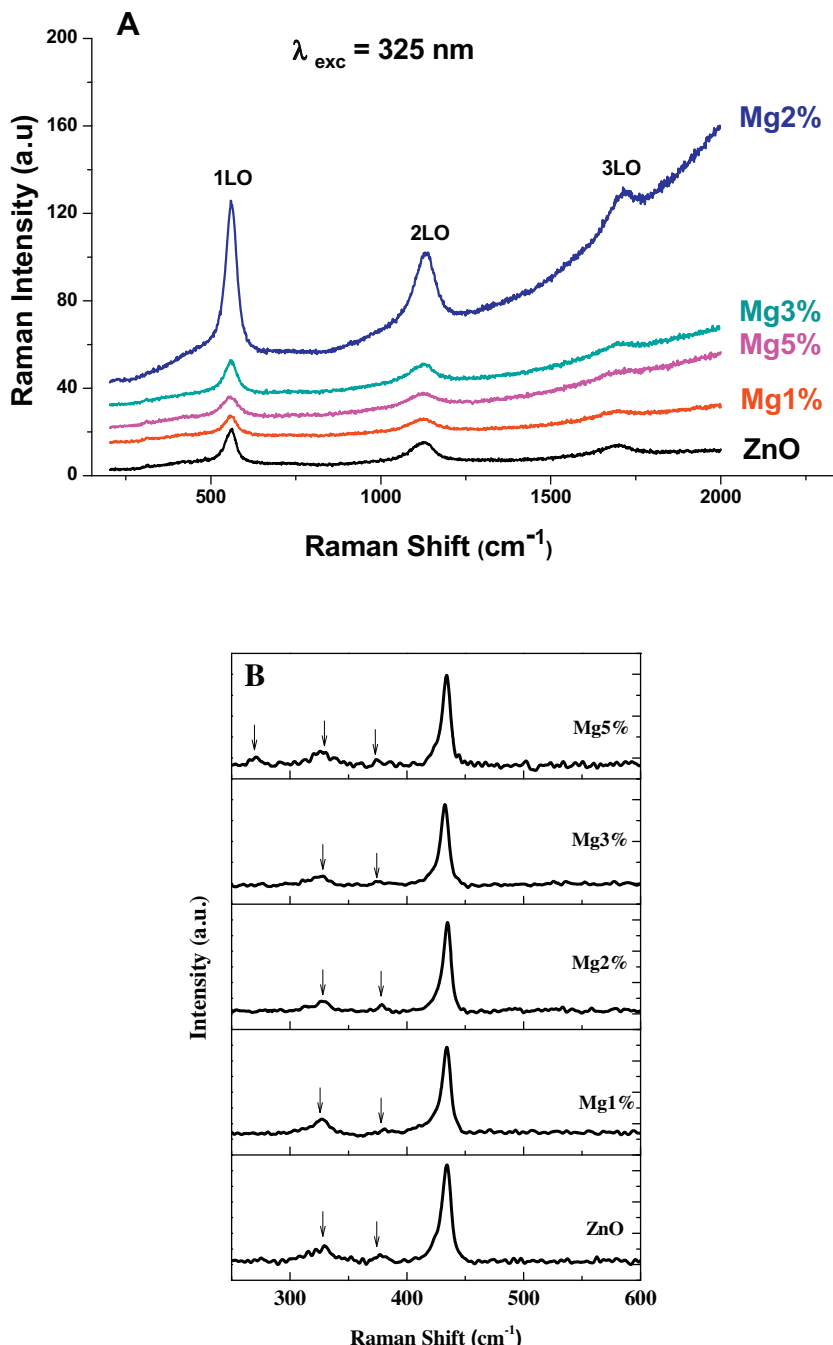


Fig. 4. Raman spectra of undoped and Mg doped ZnO NPs for the excitation wavelengths: $\lambda_{\text{exc}} = 325 \text{ nm}$ (A) and $\lambda_{\text{exc}} = 632.8 \text{ nm}$ (B).

greater than 7 nm [31]. The band Burstein–Moss effect can be at the origin of this blue shift in the optical band gap. The increase of carrier concentration in doped NCs will cause the Fermi level move into the conduction band. The filling of the conduction band by electrons will generally result in a blue shift in the near band edge emission. As the Mg content increases above 2%, more and more Mg^{2+} replace the position of Zn^{2+} , the strong sp-d exchange interaction between free charge carriers in the band of the semiconductor and the localized magnetic moments cause the absorption edge shift to the red side. It has reported that some doping elements such as Li, Ti, and Mg cause an increase in the optical band gap [32,33]. However, others doping such as Fe, Na, and Mn lead to a reduction in the optical band gap of ZnO [34–36] (Fig. 5).

The band gap is also depending on the structural disorder of semiconducting NCs which is related to the Urbach tail. Fig. 6 shows

the absorbance spectra of (2%) Mg doped ZnO sample with Urbach plot [37]. This energy is calculated using the following equation:

$$\alpha = \alpha_0 e^{(h\nu - E_g)/E_u} \quad (2)$$

where α_0 is a constant, α is the absorption coefficient, E_g is the gap energy, $h\nu$ is the incident photon energy, and E_u is the Urbach energy. The value of E_u was obtained from the inverse of the slope of $\ln(\alpha)$ versus $(h\nu)$. The band gap values were determined from the upper end of the Urbach tail. The values of E_g deduced from fits are increasing from 3.45 eV to 3.48 eV when the doping concentration increases from 0% to 2%, then it decreases up to 3.45 eV for 5% of Mg content. But, we did not see any appreciable change in the value of Urbach energy E_u .

In this study, the wider gap energy is found for the sample with the highest crystallite size which corresponds to ZnO:2%Mg

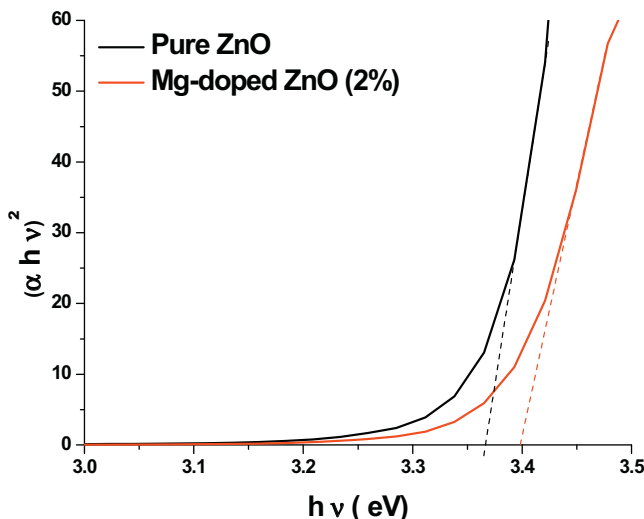


Fig. 5. The $(\alpha h\nu)^{1/2}$ versus photon energy plot of the undoped ZnO and ZnO:2%Mg NPs.

Table 4
Optical band gap of ZnO and Mg doped ZnO NPs.

Sample	ZnO	0.01-MgZnO	0.02-MgZnO	0.03-MgZnO	0.05-MgZnO
E_g (eV)	3.36	3.37	3.39	3.38	3.34

sample. The optical band gap values calculated from absorption spectra indicate that the band gap of Mg doped ZnO is wider than pure ZnO NCs for 1% and 2% of Mg content. The band gap of samples doped with 1% and 2% Mg is blue shifted; this experiment confirmed the success of doping magnesium into ZnO lattice. For higher concentrations of Mg (3% and 5%) the E_g values are decreasing, which indicate that the incorporation of Mg ions into ZnO lattice reveals new electronic states in the band gap energy.

3.4. Photoluminescence study

All the PL spectra consist of two emission bands located in UV and visible ranges (Fig. 7). The strong near-band-edge UV emission at around 377 nm, which corresponds to the band-gap energy of ZnO, is commonly attributed to the direct recombination of excitons [25]. The broad emission band located in the visible range (400–700 nm) is mainly due to point-like structural defects related to deep-level emissions, such as zinc vacancies, oxygen vacancies, interstitial zinc, and interstitial oxygen [38].

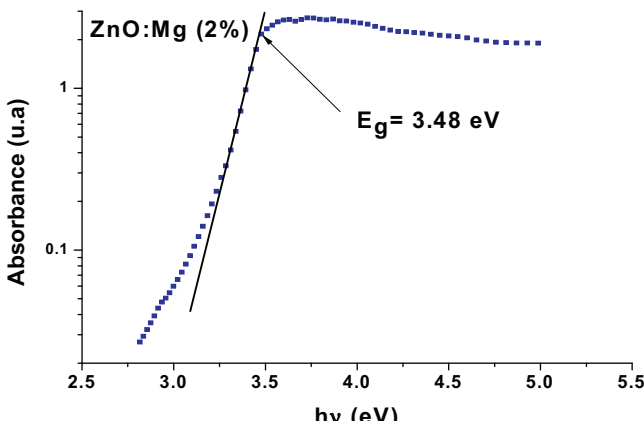


Fig. 6. Urbach plot of 0.02 MgZnO sample annealed at 500 °C.

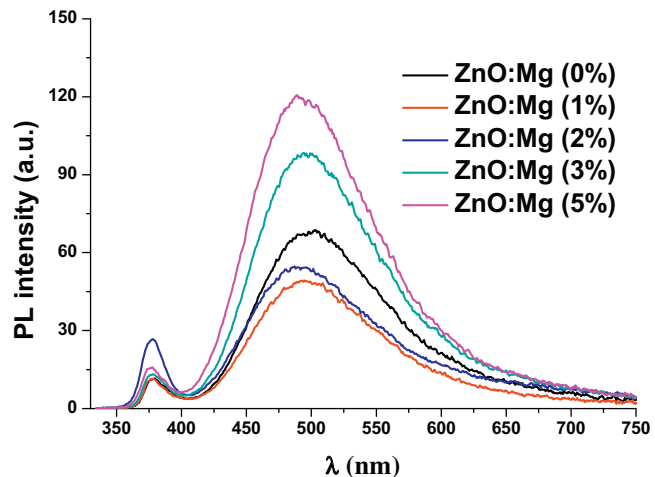


Fig. 7. Room temperature PL spectra of ZnO:Mg NPs.

No appreciable shift of near band edge with Mg doping can be shown in Fig. 7. This is in agreement with the slight variation of the optical band gap. However, we note an increase of the intensity ratio of the UV band to the visible one with Mg doping till 2%. Further doping above 2% leads to decrease of this ratio. Such behavior is in accord with stress variation in Mg doped ZnO NCs. As the stress decreases (Table 1), the ratio increases showing that low doping reduces defect density where Mg^{2+} filled Zn vacancies. However, for Mg doping above 2%, the increase of the stress is accompanied by a decrease of the ratio indicating that excess of Mg adding (above 2%) can induce structural defects. Similar behavior is reported by [39]. In other works [40,41], the increase of the intensity of the UV emission is attributed to the improved crystal quality and a decrease of the stress of ZnO due to Mg doping.

3.5. Sunlight-induced photocatalytic activity of Mg-doped ZnO

The successful synthesis of undoped and Mg doped ZnO NCs offers an opportunity to evaluate their photocatalytic activity using RhB, as test contaminant, under sunlight irradiation. RhB has been widely used as an indicator for the photocatalytic activity owing to its absorption peak in the visible range [42,43]. Fig. 8 shows the UV-visible absorption spectra of RhB in the presence of pure ZnO and (3%) Mg doped ZnO NCs at various irradiation times. The degradation was evaluated with absorption spectra by monitoring the decay of the characteristic absorption band at 554 nm as a function of exposure time. In the absence of a catalyst, the solar irradiation of RhB does not lead to any noticeable degradation. However, in the presence of pure ZnO, the characteristic absorption band of RhB decreases with increasing exposure time and the degradation is completed after 120 min. It is clear that degradation of RhB on Mg-doped ZnO NCs is greater than pure ZnO, it was occurred only about 60 min with ZnO:Mg NCs.

Fig. 9A displays the temporal course of ZnO:Mg NPs at different Mg concentrations: 0%, 1%, 2%, 3%, and 5%. All ZnO:Mg NPs present good photocatalytic activity since a quasi complete discoloration of RhB is seen. The sample ZnO:3%Mg presents the high photocatalytic activity. A similar evolution of the photocatalytic activity with Mg doping in ZnO has been reported [44].

The degradation rate is calculated using the following formula:

$$\text{Degradation rate} = \frac{A_0 - A_t}{A_0} \times 100 \quad (3)$$

where A_0 is the initial absorbance, A_t is the changed absorbance of the RhB at the characteristic absorption wavelength of 545 nm. The $\ln(A_0/A_t)$ versus time shown in Fig. 9B indicates that the

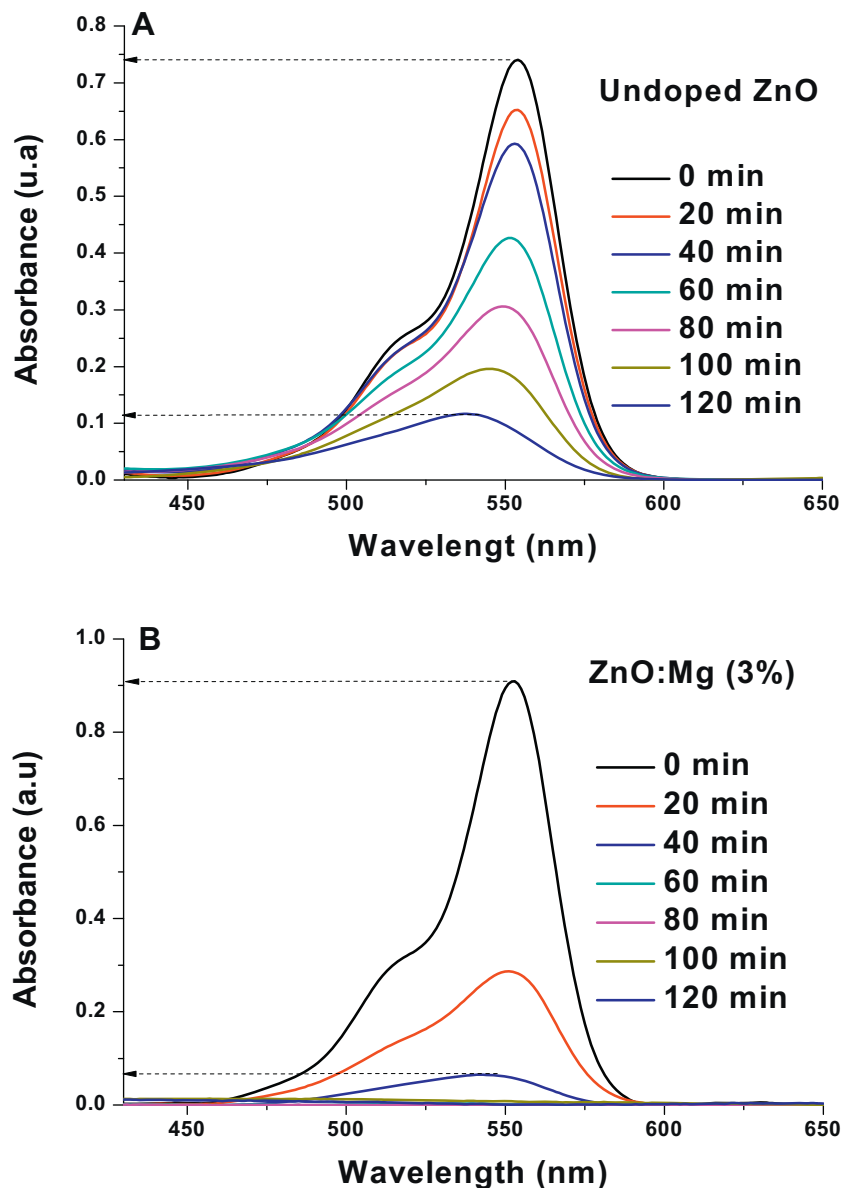


Fig. 8. (A) Absorption spectra of RhB before and after irradiation in the presence of undoped ZnO and (B) using 3%-MgZnO nanoparticles as a function of irradiation time under sunlight irradiation with catalyst (0.25 g/L), RhB (5×10^{-6} mol L⁻¹).

photo-degradation reactions of all samples roughly follow the first-order kinetic process; the corresponding degradation rate constants K [45,46] were obtained from the slope of fits.

The calculated rate constants were 6×10^{-3} min⁻¹, 26×10^{-3} min⁻¹, 13×10^{-3} min⁻¹, 41×10^{-3} min⁻¹, and 30×10^{-3} min⁻¹ for 0%, 1%, 2%, 3%, and 5% of Mg content in ZnO, respectively. The rate constants of Mg-doped ZnO give significant variation from that of undoped ZnO. So, the obtained results indicate higher performance for Mg doped ZnO in comparison to pure ZnO. Etacheri et al. [47] and Nouri et al. [48] demonstrate that Mg doped ZnO nanostructures showed a superior sunlight-induced photocatalytic decomposition of methylene blue in contrast to undoped ZnO.

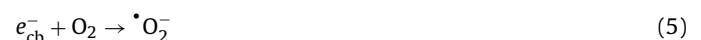
The enhanced photocatalytic activity for Mg doping above 2%, may be attributed to the large specific surface areas (since the crystallite size decreases) and surface oxygen vacancies [49].

The photocatalytic activity of semiconductors is based on the production of electron–hole pair (e^- , h^+). It depends on two processes: one is the competition between the recombination and

capture of photo-generated electrons and holes; the other is the competition between the recombination of captured electrons and holes and interface charge transfer [50]. Photocatalytic activity of undoped ZnO is attributed both to the donor states caused by the large number of defect sites such as oxygen vacancies and interstitial zinc atoms and to the acceptor states which arise from zinc vacancies and interstitial oxygen atoms [51]. In degradation of RhB, after illumination of Mg-doped ZnO NCs with sunlight irradiation, electron–hole pairs are created at the beginning of the reactions. After that, reactive species such as $\cdot\text{OH}$ and $\cdot\text{O}_2^-$ are formed by the following processes:



The photo-induced electrons are easily trapped by electronic acceptors like adsorbed (O_2), in order to produce a superoxide radical anion ($\cdot\text{O}_2^-$)



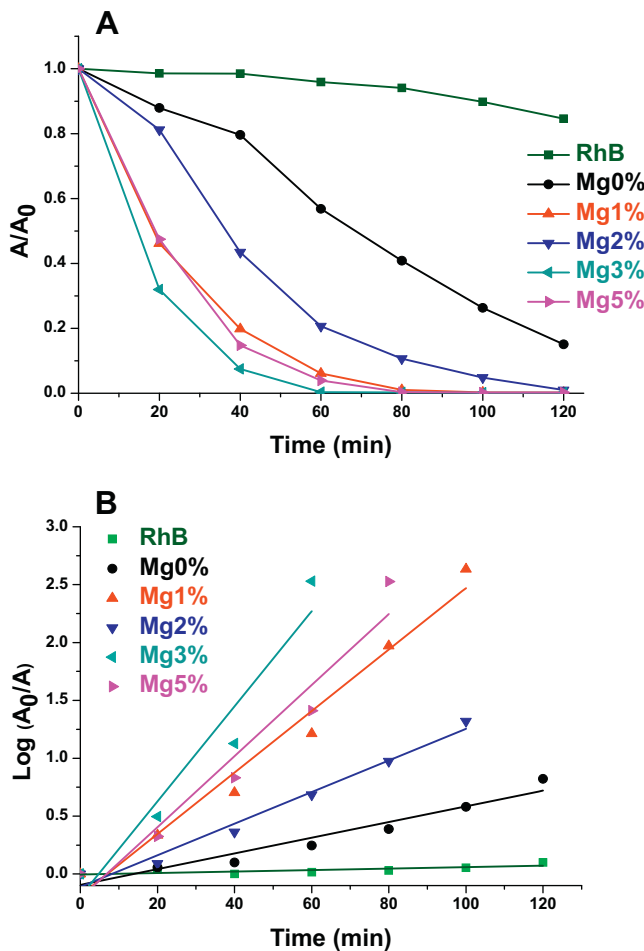
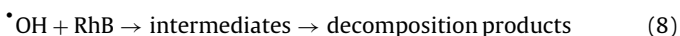
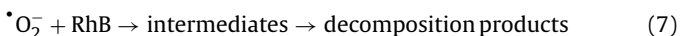


Fig. 9. (A) Relative photocatalytic activity of ZnO:Mg NPs under sun light irradiation. (B) Kinetic study of photocatalytic Rhodamine B degradation under sun-light irradiation in the presence of undoped and Mg-doped ZnO NPs.

The photo-induced holes are easily trapped by negative species (OH^-) to favor the production of hydroxyl radical species ($\cdot\text{OH}$).



The generated hydroxyl radical species and superoxide radical anion completes the global photocatalytic reaction, indeed, $\cdot\text{OH}$ is an extremely strong oxidant for the partial or complete mineralization of organic chemicals [52]. The high oxidative potential of the hole in the valence band lead to the oxidation of organic matter to reactive intermediates [53].



It is very important to prevent the recombination of electron-hole pairs in order to enhance the photocatalytic activity. Mg doped ZnO NCs, which show low UV emission, exhibit superior photocatalytic activities. All the Mg doped ZnO NCs present a considerable enhancement of the photo-degradation of the dyes compared to the undoped ZnO. So, the efficient charge separation is a critical factor responsible for the enhancement of sunlight induced photocatalytic activity.

4. Conclusion

Magnesium doped ZnO NCs were synthesized through sol-gel method. All samples exhibited pure wurtzite structure without any Mg related phases.

Both structural and optical analyses show an optimization of the ZnO crystallinity for 2%Mg doping, which is beneficial for optoelectronic application. The photocatalytic activities of ZnO: Mg samples are studied by the photodegradation of RhB under sunlight irradiation. It was found that 3%Mg doped ZnO has the highest photocatalytic activity among all samples. This shows a positive effect of Mg doping for the development of highly efficient ZnO photocatalysts with a low cost for the environmental remediation.

References

- C. Klingshirn, Phys. Stat. Sol. B 71 (1975) 547.
- H. Ohta, K. Kawamura, M. Orita, M. Hirano, N. Sarukura, H. Hosono, Appl. Phys. Lett. 77 (2000) 457.
- B.H. Lee, S.-M. Kang, Curr. Appl. Phys. 6 (2006) 844.
- D.K. Hwang, M.C. Jeong, J.M. Myoung, Appl. Surf. Sci. 225 (2004) 217.
- A. Ohotomo, M. Kawasaki, T. Koida, K. Masubuchi, H. Koinuma, Y. Sakurai, Y. Yoshida, T. Yasuda, Y. Segawa, Appl. Phys. Lett. 72 (1998) 2466.
- H.C. Hsu, C.Y. Wu, H.M. Cheng, W.F. Hsieh, Appl. Phys. Lett. 89 (2006) 13101.
- T.H. Fang, S.H. Kang, J. Appl. Phys. 105 (2009) 113512.
- T. Makino, N.T. Tuan, H.D. Sun, C.H. China, Y. Segawa, M. Kawasaki, A. Ohotomo, K. Tamura, T. Suemoto, H. Akiyama, M. Baba, T. Tomita, H. Koinuma, Appl. Phys. Lett. 78 (2001) 1979.
- K. Ogata, K. Koike, T. Tanite, T. Komuro, F. Yan, S. Sasa, M. Inoue, M. Yano, J. Cryst. Growth 251 (2003) 623.
- W.I. Park, G.C. Yi, H.M. Jang, Appl. Phys. Lett. 79 (2001) 2022.
- P. Wang, N. Chen, Z. Yin, R. Dai, Y. Bai, Appl. Phys. Lett. 89 (2006) 202102.
- P.P. Sahay, S. Tewari, R.K. Nath, Cryst. Res. Technol. 42 (2007) 723.
- E. Bellingeri, D. Marre, I. Paluszak, L. Pellegrino, G. Canu, A.S. Siri, Thin Solid Films 486 (2005) 186.
- C.W. Lin, T.Y. Cheng, L. Chang, J.Y. Juang, Phys. Stat. Sol. (c) 1 (2004) 851.
- M. Fahoume, O. Maghfoul, M. Aggour, B. Hartiti, F. Chraibi, A. Ennaoui, Sol. Energy Mater. Sol. Cells 90 (2006) 1437.
- G. Srinivasan, J. Kumar, Cryst. Res. Technol. 41 (2006) 893.
- F.M. Moghaddam, H. Saeidian, Mater. Sci. Eng. B 139 (2007) 265.
- A. Tabib, N. Sdiri, H. Elhouichet, M. Férid, J. Alloys Compd. 622 (2015) 687.
- A.K. Zak, W.H.A. Majid, M.E. Abrishami, R. Yousefi, Solid State Sci. 13 (2011) 251.
- R. Chauhan, A. Kumar, R.P. Chaudharya, J. Chem. Pharm. Res. 2 (4) (2010) 178.
- V.D. Mote, Y. Purushotham, B.N. Dole, J. Theor. Appl. Phys. 6 (2010) 6.
- G. Xiong, U. Pal, J. Garcia Serrano, J. Appl. Phys. 101 (2007) 024317.
- R.P. Wang, G. Xu, P. Jin, Phys. Rev. B 69 (2004) 113303.
- K. Ishikawa, N. Fujima, H. Komura, J. Appl. Phys. 57 (1985) 973.
- W. Bousslama, H. Elhouichet, B. Gelloz, B. Sieber, A. Addad, M. Moreau, M. Férid, N. Koshida, Jpn. J. Appl. Phys. 51 (2012) 04DG13.
- B.H. Bairamov, A. Heinrich, G. Irmer, V.V. Toporov, E. Ziegler, Phys. Status Solidi B 119 (1983) 227.
- K. Samanta, P. Bhattacharya, R.S. Katiyar, W. Iwamoto, P.G. Pagliuso, C. Rettori, Phys. Rev. B 73 (2006) 245213.
- F.J. Manjón, B. Mari, J. Serrano, A.H. Romero, J. Appl. Phys. 97 (2005) 053516.
- M. Nowak, B. Kauch, P. Szperlich, Rev. Sci. Instrum. 80 (2009) 46107.
- M. Girtan, G. Folcher, Surf. Coat. Technol. 172 (2003) 242.
- E.A. Meulenkamp, J. Phys. Chem. B 102 (1998) 5566.
- M. Caglar, Y. Caglar, S. Aksoy, S. Ilcan, Appl. Surf. Sci. 256 (2010) 4966.
- S. Suwanboon, P. Amornpitoksuk, A. Sukolrat, Ceram. Int. 37 (2011) 1359.
- M. Mehedi Hassan, W. Khan, A. Azam, A.H. Naqvi, J. Lumin. 145 (2014) 160.
- S. Ilcan, J. Alloys Compd. 553 (2013) 225.
- Y. Caglar, S. Ilcan, M. Caglar, F. Yakuphanoglu, J. Sol-Gel Sci. Technol. 53 (2010) 372.
- G. Liu, Z. Chen, C. Dong, Y. Zhao, F. Feng Li, G.Q. Lu, H.-M. Cheng, J. Phys. Chem. B 110 (2006) 20823.
- H. Zeng, G. Duan, Y. Li, S. Yang, X. Xu, W. Cai, Adv. Funct. Mater. 20 (2010) 561.
- R. Yousefi, A.K. Zak, F. Jamali-Sheini, Mater. Sci. Semicond. Process. 16 (2013) 771.
- X. Long, X. Li, P.T. Lin, X.W. Cheng, Y. Liu, C.B. Cao, Chin. Phys. B 19 (2010) 027202.
- L. Xu, J. Su, Y. Chen, G. Zheng, S. Pei, T. Sun, J. Wang, M. Lai, J. Alloys Compd. 548 (2013) 7.
- R. Nagaraja, N. Kagaraju, C.R. Girija, B.M. Nagabhushana, Powder Technol. 215 (2011) 10.
- A.B. Patil, K.R. Patil, S.K. Pardeshi, J. Hazard. Mater. 183 (2010) 315.
- C. Liu, F. Shang, G. Pan, F. Wang, Z. Zhou, W. Gong, Z. Zi, Y. Wei, X. Chen, J. Lv, G. He, M. Zhang, X. Song, Z. Sun, Appl. Surf. Sci. 305 (2014) 753.
- M. Rezaei, A. Habibi-Yangjeh, Appl. Surf. Sci. 265 (2013) 591.

- [46] I.K. Konstantinou, T.M. Sakellarides, V.A. Sakkas, T.A. Albanis, Environ. Sci. Technol. 35 (2001) 398.
- [47] V. Etacheri, R. Roshan, V. Kumar, J. ACS Appl. Mater. Interfaces 4(5) (2012) 2717.
- [48] H. Nouri, A. Habibi-Yangjeh, Adv. Powder Technol. 25 (2014) 1016.
- [49] L. Zhang, L. Yin, C. Wang, N. Lun, Y. Qi, ACS Appl. Mater. Interfaces 2 (2010) 1769.
- [50] X. Bai, N. Pan, X. Wang, H. Wang, J. Phys. Chem. C 21 (2008) 81.
- [51] F. Tuomisto, K. Saarinen, Phys. Rev B 72 (2005) 085206.
- [52] H.C. Yatmaz, A. Akyol, M. Bayramoglu, Ind. Eng. Chem. Res. 43 (2004) 6035.
- [53] D. Monllor-Satoca, R. Gómez, M. González-Hidalgo, P. Salvador, Catal. Today 129 (2007) 247.